ACS OMEGA

Open Access

http://pubs.acs.org/journal/acsodf

Article

Experimental Study on the Improvement of Char Physicochemical Properties and Reactivity by Activation Process in CFB

Siyuan Zhang, Mingyue Wang, Chen Liang,* and Zhiping Zhu

Cite This: *ACS Omega* 2024, 9, 24500−24512

Read Online

ACCESS | Metrics & More | Article Recommendations

ABSTRACT: Solid carbon can be transformed into activated char with higher reactivity through the activation process in a circulating fluidized bed (CFB) to improve the Boudouard reaction. A new technology for reducing CO_2, the activated-reduction technology, was proposed. In order to investigate the influence of relevant parameters (carbon dioxide addition, oxygen concentration, and O_2/C) of the activation process on the physicochemical properties and reactivity of activated char, the experiments were carried out on a bench-scale CFB. The relationship between the parameters and the reactivity of activated char is explored. The result shows that compared with the raw coal, the pore structure of activated char is developed, the number of active sites increases, the degree of graphitization decreases, and higher reactivity is possessed. For the activation process, less of the O_2/C and moderate oxygen concentration promote the increase in activated char reactivity, which is conducive to the reduction of CO_2. The results of the correlation discussion show that the reactivity is difficult to be characterized by a single simple parameter. The reactive specific surface area (*RSSA*) obtained by multiplying the mesoporous specific surface area and I_{D3+D4}/I_{all} has a good effect on describing the reactivity.

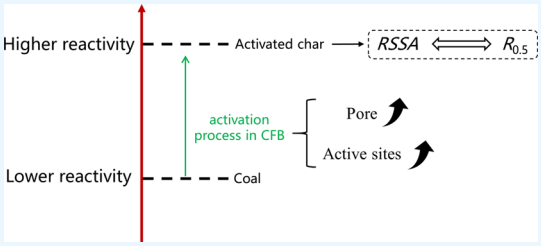

1. INTRODUCTION

Climate change is widely recognized as a consequence of increased emissions of anthropogenic greenhouse gases (GHGs) resulting from rapid economic growth.[1,2] Among these GHGs, carbon dioxide (CO_2) stands out as the primary greenhouse gas emitted through human activities. Carbon monoxide (CO) is an important precursor and intermediate chemical for deriving a wide range of commodity chemicals.[3] The reduction of CO_2 can be achieved by gasification technology to produce CO-rich syngas, which offers the potential for CO_2-to-chemicals transformation and waste-to-wealth strategies.[4]

During the gasification process, CO_2 is primarily reduced through the Boudouard reaction ($CO_2 + C \rightarrow 2CO$). The free energy change of the Boudouard reaction becomes negative beyond 700 °C, making CO formation progressively favored.[5] However, its reaction rate is still slow due to the chemical stability of CO_2.[1,6] Therefore, it is crucial to improve the intensity of the Boudouard reaction for effective utilization of CO_2 through the gasification process. Generally, the Boudouard reaction can be enhanced by increasing temperature or CO_2 partial pressure.[7] In addition, as a heterogeneous reaction, the Boudouard reaction can be enhanced by increasing the chemical reactivity of solid carbon. According to those published reviews on CO_2 utilization in thermochemical conversion,[4,8] it is confirmed that solid carbon properties have an important effect on the Boudouard reaction.

The increase in the chemical reactivity of solid carbon can be achieved through the partial gasification process, which includes pyrolysis reactions, combustion reactions, and gasification reactions, in the circulating fluidized bed (CFB) reactor.[9,10] Activated char obtained from the CFB partial gasification process exhibits notable improvements compared to raw materials, including a larger specific surface area, better pore structure development, reduced graphitization, and a higher concentration of defective carbon site.[10−12] These changes contribute to a higher CO_2 reduction capability of the char. Su et al.[13] demonstrated that the specific surface area, pore volume, and pore diameter of char were larger than those of raw coal, suggesting that the partial gasification process in CFB optimizes the pore structure. Ding et al.[14] investigated the microstructure of char derived from CFB gasification and observed a decrease in graphitization and a conversion of the stable graphite structure into a disordered defective structure in the carbon frame. Qi et al.[15] investigated the activation performance of coal gasification fly ash using a bench-scale CFB under an oxygen/steam atmosphere, resulting in a

Received: January 15, 2024
Revised: May 11, 2024
Accepted: May 14, 2024
Published: May 28, 2024

maximal increase of 48.9% in the specific surface area of the activated gasification fly ash. Liang et al. compared the activity of char from air gasification and oxygen/steam gasification processes.[9] It is found that the steam gasification reaction could increase the formation of active carbon sites.

In this context, the Institute of Engineering Thermophysics, Chinese Academy of Sciences (IET, CAS), has developed the activated-reduction technology for CO_2 reduction, which utilizes a combination of CFB and a downdraft reactor (DR). The schematic diagram of activated-reduction technology is shown in Figure 1. The solid carbon is activated in CFB

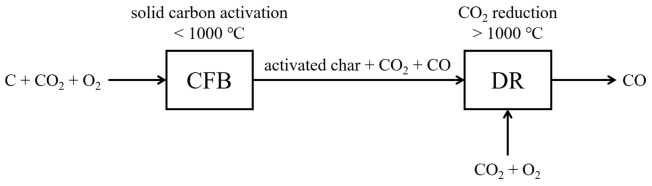

Figure 1. Schematic diagram of activated-reduction technology.

and converted to activated char. DR provides a higher temperature (>1000 °C) to promote the reduction of CO_2 to CO by activated char. The temperature of the DR depends on the oxygen flow fed into the DR. The activated char with better reactivity may favor a lower temperature to reduce CO_2. Therefore, the reactivity of activated char from CFB significantly impacts the reduction of CO_2. Hence, it is crucial to investigate the microscopic effects of CFB on activated char to assess the feasibility of CO_2 reduction.

Raman spectroscopy and X-ray diffraction (XRD) have been widely employed to investigate the structural features of char.[8] Liu et al.[11] conducted a study using Raman spectroscopy to examine the carbon structure properties of coal and char obtained from coal gasification under an O_2/CO_2 atmosphere. Their findings provided insights into the reduction in char graphitization compared with raw coal. In a similar vein, Zhang et al.[10] utilized Raman spectroscopy to compare the differences between raw coal and air gasification char, highlighting a decrease in char graphitization. Li et al.[16] focused on investigating the interlamellar spacing of atmospheric CFB coal gasification fly ash through XRD analysis. Yang et al.[17] used XRD and Raman spectroscopy to analyze the carbon structure of coal gasification fly ash from the CFB gasifier and found abundant amorphous carbon structure in the fly ash. Jiang et al.[18] employed XRD and Raman spectroscopy to explore the molecular structure of bituminous coal, examining four coal samples sourced from coal mines in the northern region.

Previous research has shown that the CFB gasification process can activate solid carbon and improve its reactivity. Therefore, it is crucial to investigate the microscopic effects of CFB on activated char to assess the feasibility of CO_2 reduction. In this work, bituminous coal and a bench-rig CFB test system were used to analyze the improvement effect of the CFB thermal activation process. The char from the CFB is named activated char. In order to comprehensively evaluate the activation process, the influence of various operating parameters (including the active agent, O_2 concentration, and O_2/C) on the activation effect was examined. The relationship between the activated char properties and the Boudouard reaction rate was further analyzed to establish the relation between the activation process and the CO_2 reduction effect. Finally, the correlation between the parameters employed and the reactivity of activated char was examined.

2. EXPERIMENTAL SECTION

2.1. Fuel Characteristics. Shenmu bituminous coal (SM) was used as the raw material. The proximate and ultimate analyses are shown in Table 1. Particle size distributions of SM are shown in Figure 2. The particle size distribution diagram of SM shows that the cumulative volume fractions of 10, 50, and 90% with particle sizes are 72.71, 293.4, and 585.4 μm, respectively.

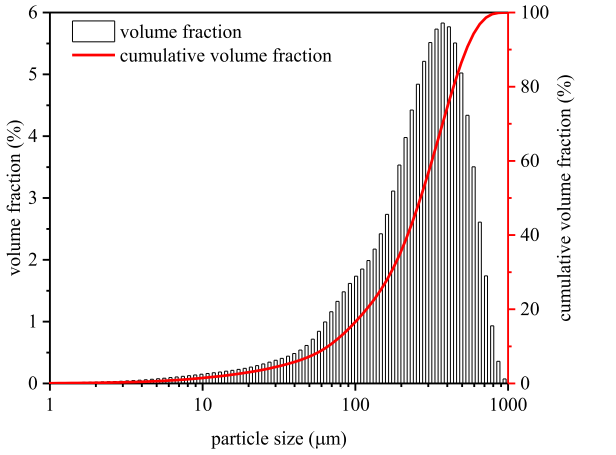

Figure 2. Particle size distributions of SM.

2.2. Test Rig. The experimental setup utilized a 20 kg/h gasification rig to conduct the study (Figure 3). The rig consists of interconnected components, including a CFB unit and associated auxiliary systems. The CFB unit serves as the activation unit. The CFB unit comprises a riser, a cyclone separator, and a loop seal. The riser has an inner diameter of 140 mm and a height of 3 m. The active agent was fed into the riser from the bottom, including air, nitrogen, oxygen, and carbon dioxide. Air was supplied by an air compressor. Nitrogen, oxygen, and carbon dioxide were supplied by the gas stations. Before entering the riser, the active agent (except for oxygen) was first heated to 300 °C in the gas preheater.

In this study, seven cases were realized, and the operating parameters are shown in Table 2. Before the experiments began, 15 kg quartz sand with a particle size of 0.212−0.425 mm was fed into the riser and used as bed material. When the experiments began, the CFB was first heated up by an electrical heater, and the gas preheater was turned on. At the same time, a small amount of air was injected into the riser to fluidize the

Table 1. Proximate and Ultimate Analysis (wt %, Arrived Basis) of SM

proximate analysis (wt %)				ultimate analysis (wt %)					low calorific value (MJ/kg)
M_{ar}	A_{ar}	V_{ar}	FC_{ar}	C_{ar}	H_{ar}	N_{ar}	S_{ar}	O_{ar}	$Q_{net,ar}$
7.50	5.76	35.19	51.55	69.52	4.50	1.10	0.39	11.23	26.99

https://doi.org/10.1021/acsomega.4c00467
ACS Omega 2024, 9, 24500−24512

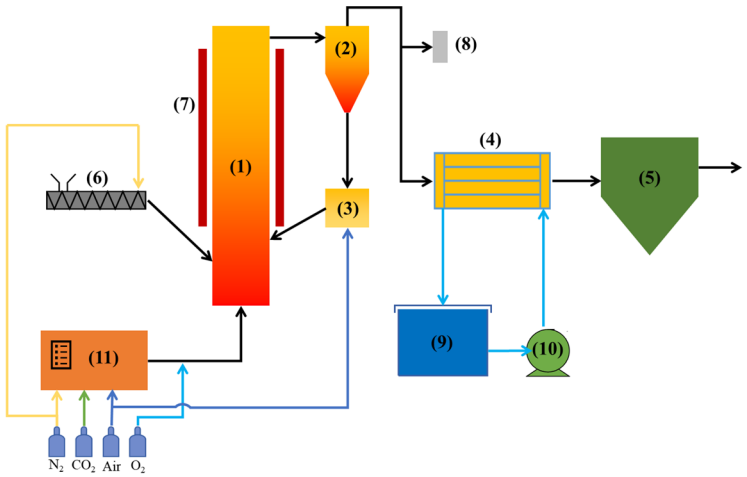

1. riser; 2. cyclone; 3. loop seal; 4. gas cooler; 5. bag filter; 6. screw feeder; 7. electrical heater; 8. product sampling point; 9. water tank; 10. water pump; 11. gas preheater;

Figure 3. Schematic diagram of the test rig.

Table 2. Operating Conditions Related to the Activation Process

	temperature (°C)					
	CFB bottom	loop seal	fluidizing gas velocity (m/s)	total pressure drops in riser (kPa)	active agent composition	O_2/C (mol/mol)
OC1	~928	~903	~1.69	~6.21	air	~0.26
OC2	~920	~896	~2.28	~5.46	O_2/CO_2 (22%/78%)$_{vol}$	~0.26
OC3	~923	~895	~1.56	~4.33	O_2/CO_2 (32%/68%)$_{vol}$	~0.25
OC4	~921	~871	~0.87	~6.75	O_2/CO_2 (41%/59%)$_{vol}$	~0.26
OC5	~924	~855	~1.13	~7.85	O_2/CO_2 (50%/50%)$_{vol}$	~0.25
OC6	~928	~888	~1.15	~7.77	O_2/CO_2 (38%/62%)$_{vol}$	~0.35
OC7	~925	~872	~1.11	~7.89	O_2/CO_2 (39%/61%)$_{vol}$	~0.45

bed material. When the bottom of the riser was heated up to 650 °C, the coal was fed into the riser and combusted to improve the temperature. At this time, the air in the riser should be excessive for coal combustion, ensuring that the gas out of CFB contains oxygen. When the temperature at the bottom of the riser reached 850 °C, the coal feed was increased and the active agent was adjusted to the operating conditions. Finally, the coal feed, active agent, and electrical heater power were adjusted to achieve stable operation of the test rig. When the temperature variation of the CFB bottom was less than ±4 °C in 10 min, the operating condition was considered stable. One operating condition was that it remained for over 1 h, during which activated char and gas were collected at the outlet of the CFB. The activated char obtained in OC1 to OC7 were named AC1 to AC7 respectively. The difference between the temperature of the loop seal and the temperature of the CFB bottom is small, which can indicate that the operating status is in a high gas velocity circulation regime.

O_2/C (mol/mol) in Table 2 is calculated by eq 1:

$$O_2/C = \frac{y_{O_2}}{C_{ar}} \cdot \frac{12}{22.4} \quad (1)$$

where y_{O2} is the volume of O_2 into the system per unit mass of coal (Nm^3/kg); C_{ar} is carbon content (wt %) in the feedstock arrived basis.

2.3. Sample Analytical Methods. The pore structure and specific surface area of the solid samples were analyzed. CO_2 and N_2 were used as adsorption media to measure the pore structure and specific surface area of the particles, respectively, using the NOVA 2000e from Quantachrome USA for CO_2 adsorption and the autosorb iQ from Quantachrome USA for N_2 adsorption. The bath temperatures of CO_2 and N_2 were 273 and 77.3 K, respectively. For the N_2 adsorption results, the BET method was used to calculate the specific surface area of the sample mesopores, and the BJH (Barrett−Joyner−Halenda) model was used to calculate the specific mesopores pore volume.[19] For the CO_2 adsorption results, the DFT method was used to calculate the specific surface area of the micropores, and the SF (Saito−Foley) model was used to calculate the micropore-specific pore volume.

Raman testing of samples was carried out using Renishaw inVia equipment. The excitation wavelength was 532 nm, and the recording range was 2000−800 cm^{-1}, covering first-order bands. The Raman results were analyzed using the split-peak fit, divided into five peaks for the fit, containing one Gaussian peak (D_3 band) and four Lorentzian peaks (G, D_1, D_2, and D_4 band).[14] The 1350, 1620, 1530, 1150, and 1580 cm^{-1} were respectively D_1, D_2, D_3, D_4, and G band.[20,21] In Raman spectroscopy, the intensity ratio of the D_1 band to the G band has been proved to correlate well with the degree of carbon structural order, and the D_3 and D_4 bands may be responsible for the reacting sites.[22,23] The peak area ratios I_G/I_{all}, I_{D1}/I_G, and $I_{(D3+D4)}/I_G$ are usually used to analyze the carbon structure.[10,22]

XRD was carried out using an X-ray diffractometer from Empyrean of PANalytical B.V., Holland. Detection range 5° to 90°, Cu target. XRD results were processed by a peak-splitting fitting. The broad hump was fitted to three peaks around 21°, 26°, and 43°, representing γ peak, 002 peak, and 100 peak,

https://doi.org/10.1021/acsomega.4c00467
ACS Omega 2024, 9, 24500−24512

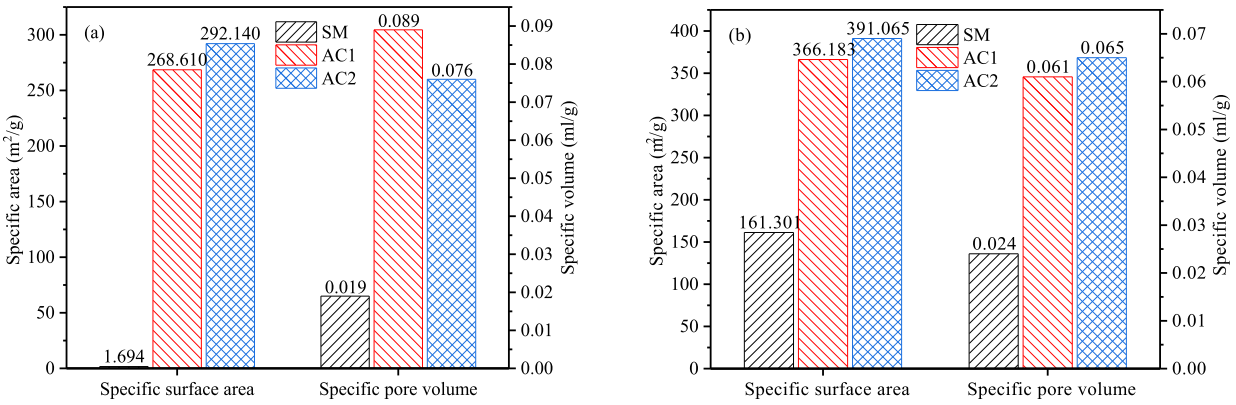

Figure 4. Specific surface area and the specific pore volume of SM, AC1, and AC2 (a) mesopore, (b) micropore.

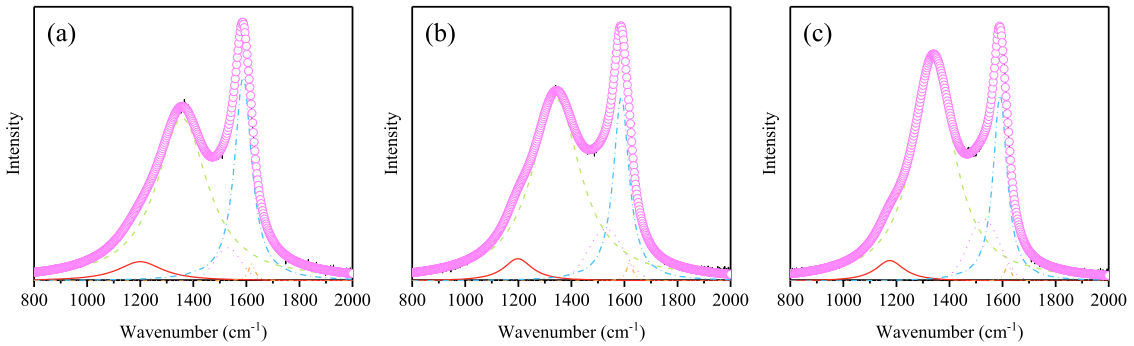

Figure 5. Raman spectra of SM (a), AC1 (b), and AC2 (c).

respectively. The interlayer spacing of aromatic layers (d_{002}) was calculated from peak 002 position by Bragg's equation.[24] The average stack height of the aromatic layer (L_c) and the average string length of the aromatic layer (L_a) were obtained from the Scherrer formula.[25] The average number of layers per stack (N) was calculated by L_c and d_{002}. The equations of L_a, L_c, d_{002}, and N are shown in eqs 2−5, respectively.[26]

$$L_a = \frac{1.84\lambda}{\beta_{100}\cos(\theta_{100})} \tag{2}$$

$$L_c = \frac{0.89\lambda}{\beta_{002}\cos(\theta_{002})} \tag{3}$$

$$d_{002} = \frac{\lambda}{2\sin(\theta_{002})} \tag{4}$$

$$N = \frac{L_c}{d_{002}} \tag{5}$$

where λ is the wavelength of the incident X-rays (0.1540598 nm), β is the half-width at peak maximum (rad) and θ is the Bragg angle (in rad).

The CO_2 reactivity of the samples was performed on STA 449 F3 TGA from NETZSCH, Germany. The test of the CO_2 reactivity of samples steps was as follows:

1. Loaded approximately 15 mg of sample into the device
2. After the sample was loaded into the equipment, nitrogen was injected to purge for 1 h, and other gases in the sample room are eliminated
3. The temperature rose to 900 °C at 20 K/min, during which N_2 was continuously injected
4. After the temperature rose to 900 °C, the temperature was kept for 5 min and then CO_2 was injected
5. When the weight of the sample was no longer changing, the cooling down procedure began.

The carbon conversion x and gasification rate r are calculated using the eqs 6 and 7, respectively.[27]

$$x = \frac{m_0 - m_t}{m_0 - m_{ash}} \times 100\% \tag{6}$$

$$r = -\frac{1}{m_0 - m_{ash}}\frac{dm}{dt} \tag{7}$$

where m_0 is the initial mass of char, m_t is the char mass at time t, and m_{ash} is the mass after gasification has been completed.

3. RESULTS AND DISCUSSION

3.1. Effect of CO_2 on the Activation Process. Experiments OC1 and OC2 were carried out to study the effect of CO_2 on the activation process by employing air and O_2/CO_2, respectively. The OC1 and OC2 were operated with the bottom temperature of riser stabilized around 928 and 920 °C, respectively, and the O_2/C of the active agent was 0.26.

The specific surface area and specific pore volume of raw coal and activated char are shown in Figure 4. The specific surface area and specific pore volume of the mesopores and the micropores in activated char are much higher than those of SM. During the activation process, the raw coal undergoes a significant transformation into activated char with well-developed mesopores and micropores. This information on pore structure is partially attributed to the rapid thermal decomposition of volatile components during activation. It leads to the removal of internal pore blockages caused by side

https://doi.org/10.1021/acsomega.4c00467
ACS Omega 2024, 9, 24500−24512

chain groups. Moreover, the gasification reactions occurring during the activation process further contributed to the enlargement and expansion of internal pores in the particles. In comparison to air as the active agent, the activated char exhibits a slightly larger specific surface area when O_2/CO_2 was used as the active agent, although the pore volume of mesopores was relatively smaller. The Boudouard reaction is strengthened by a higher CO_2 concentration in O_2/CO_2 and the internal pore blockages carbon is removed, which favors the formation of pores.

The Raman spectra of SM, AC1, and AC2 are shown in Figure 5. The variation of band area ratios of SM, AC1, and AC2 based on the results of the split-peak fit is shown in Figure 6. The I_{D1}/I_G and I_{D3+D4}/I_G of AC1 and AC2 are higher than

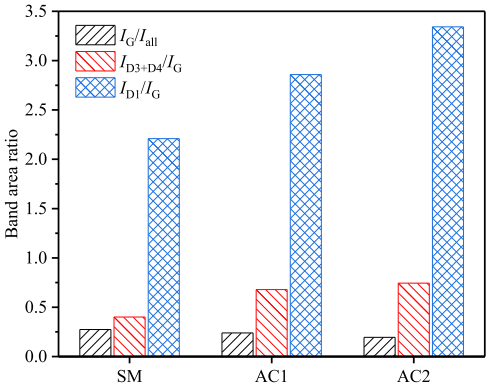

Figure 6. Variation of band area ratios of SM, AC1, and AC2.

those of SM, while the I_G/I_{all} is lower than that of SM. These observations suggest that the activated char exhibits a higher proportion of defect and a lower percentage of stable graphite structure compared to the SM. Furthermore, a comparison between AC1 and AC2 indicates that the addition of CO_2 as an active agent has a promoting effect on the activation process. This effect can be attributed to the Boudouard reaction promoting the transformation of the graphite structure to the active sites.

Figure 7 shows the XRD patterns of samples. The sample spectra show broader diffraction peaks at around 24° and 43°, indicating a lower degree of graphitization of the SM, AC1, and AC2. The 002 peak (around 26°) is not symmetrical due to the presence of the γ band (around 21°) produced by the amorphous carbon, and the presence of the γ band can be ascribed to an amorphous carbon.[16] The diffraction spectrum of the raw coal exhibits a less prominent 100 peak (around 43°) compared with the activated char, indicating a correlation with the size of the aromatic sheet. The crystal lattice parameters of the samples are presented in Figure 8. The activation process leads to an increase in the average string length of the aromatic layer while reducing the average stacking height of the aromatic layer and the average number of layers per stack. The interlayer spacing of the aromatic layers changes little due to the relatively low activation temperature employed in this study. The introduction of CO_2 further amplifies these trends.

Considering that heat treatment is involved in the activation process, the condensation of aromatic layers contributes to the expansion of aromatic layers. Concurrently, carbon atoms are consumed by the active agent, leading to a decrease in the number of aromatic layers. Moreover, the aromatic layer is further diminished by the enhanced Boudouard reaction when CO_2 is introduced of enhances.

The thermogravimetric experimental results for the samples are presented in Figure 9. The reactivity of activated char is better than that of raw coal, indicating that the activation process promotes the improvement of char reactivity. Upon comparison of the thermogravimetric results of AC1 and AC2, it can be observed that the addition of CO_2 further enhances the effect of the activation process, which is consistent with the findings from Raman spectroscopy and pore structure results. The improvement of porous structure and the decrease in graphitization contribute to increasing the reactivity of activated char. Considering the XRD results, while the L_a of the feedstock increases during the activation process, it does not prevent the reactivity of the activated char from increasing.

3.2. Effect of Oxygen Concentration on Activated Char. The effect of the oxygen concentration in the active agent on the activated char is investigated by analyzing activated char (AC2 ~ AC5). Since O_2/CO_2 is used as the active agent, the effect of the change in the concentration of CO_2 should also be considered. Figure 10 presents the specific surface area and specific pore volume of activated char obtained from different oxygen concentration conditions. As the oxygen concentration increases, there is a gradual decrease in the specific surface area and the specific pore volume of micropores of activated char. This situation indicates that the formation and development of micropores of activated char are favored by lower oxygen concentration. As the oxygen concentration decreases, there is a corresponding increase in the CO_2 concentration. The higher CO_2 concentration facilitates the diffusion of CO_2 in the activated char, resulting in an expanded region where the Boudouard reaction occurs and an increased reaction intensity in the activated char. The formation and development of micropores in activated char are promoted by the enhanced Boudouard reaction.

The Raman spectra are fitted in the same way as in section 3.1, and the results are shown in Figure 11. The I_G/I_{all} of activated char gradually increases as the oxygen concentration in the active agent increases, implying a gradual but not significant increase in the level of graphitization of activated char. As the oxygen concentration increases, I_{D3+D4}/I_G increases and then decreases. When the oxygen concentration reaches 41%, I_{D3+D4}/I_G reaches its maximum value. The trend in I_{D1}/I_G is the opposite. As the oxygen concentration increases, I_{D1}/I_G decreases and then increases. When the oxygen concentration reaches 41%, I_{D1}/I_G reaches the minimum value. This suggests that as the oxygen concentration in the active agent increases, the number of active sites first increases and then decreases relative to the percentage of graphitized carbon crystals. The reacting sites are represented by amorphous carbon present as sp^2 hybridization in activated char and mixed sp^2−sp^3 bond sites at the edges of the carbon crystals.[28,29] This is likely due to the Boudouard reaction promoting the formation of active sites represented by D_3 and D_4. However, the intense combustion reactions corresponding to the high oxygen concentration promote the disappearance of the active sites. The percentage of in-plane imperfections, such as defects and heteroatoms, in the graphite lattice, corresponding to the D_1 band decreases with increasing oxygen concentration.[21,30] This phenomenon suggests that an increase in oxygen concentration led to a more regular graphite structure in activated char.

https://doi.org/10.1021/acsomega.4c00467
ACS Omega 2024, 9, 24500−24512

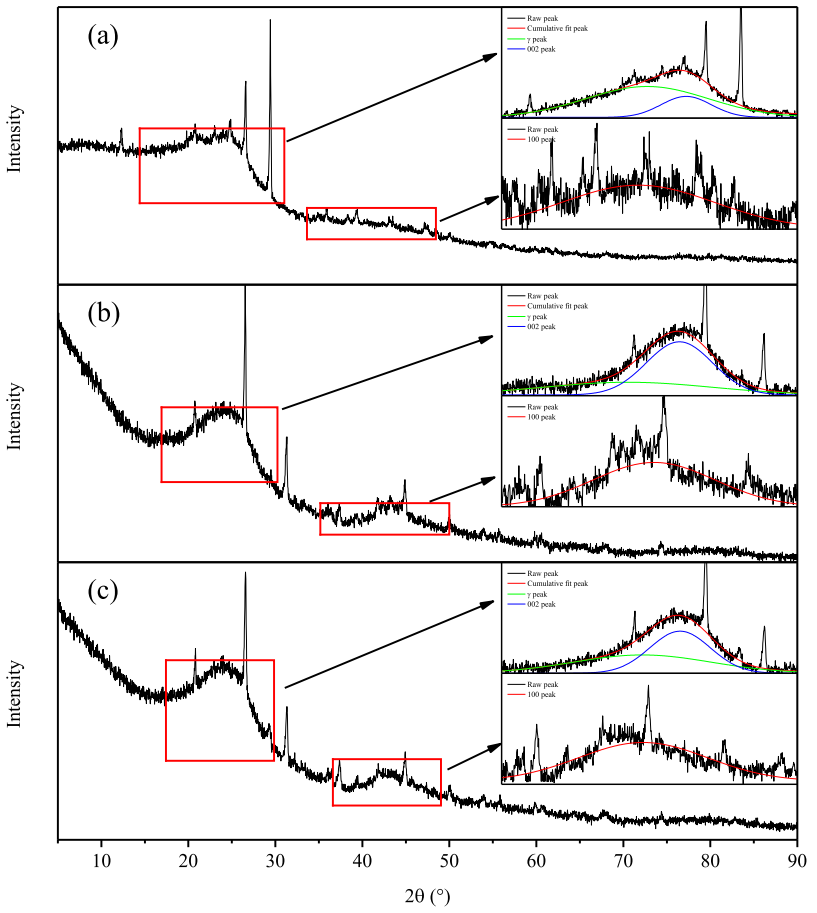

Figure 7. XRD pattern of SM (a), AC1 (b), and AC2 (c).

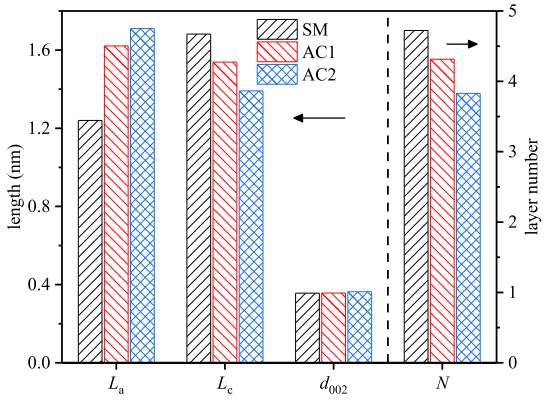

Figure 8. Crystal lattice parameters of SM, AC1, and AC2.

The XRD results are processed in the same way as in Section 3.1, and the results are shown in Figure 12. L_a, L_c, and N exhibit a gradual increase with adding oxygen concentration, while d_{002} decreases. The observed increase in oxygen concentration corresponds to enhanced graphitization of activated char, aligning with the findings from the Raman spectroscopy results. Considering that the O_2/C ratio remains constant, the consumption of carbon atoms in activated char by oxygen is essentially unchanged. Conversely, the decrease in oxygen concentration, accompanied by an elevation in CO_2 concentration, intensifies the Boudouard reaction. This promotes the conversion of carbon atoms to CO, resulting in a reduction in L_a, L_c, and N.

Figure 13 shows the thermogravimetric experiment results for activated char obtained under different oxygen concentration conditions. Among these, AC4 exhibits the highest reactivity, followed by AC2, while AC3 and AC5 display comparable reactivity. The thermogravimetric experiment results align closely with the specific surface area and specific pore volume of mesoporous of activated char. However, the correlation with micropores appears less evident. It might be likely attributed to the fact that mesoporous particles predominantly govern CO_2 diffusion in activated char. Notably, the mesoporous parameters of AC2 and AC4 exhibit similarity, yet a discernible disparity in reactivity, potentially attributed to carbon structural variations in activated char. Notably, AC4 demonstrates a significantly higher number of active sites compared with AC2, a phenomenon substantiated by the I_{D3+D4}/I_G ratio in Raman spectroscopy. This observation implies that D_3 and D_4 correspond to active sites, corroborating findings from previous research endeavors.[21,28]

3.3. Effect of O_2/C on Activated Char. The effect of O_2/C in the active agent on activated char is investigated by analyzing solid samples obtained from OC4, OC6, and OC7 (corresponding to AC4, AC6, and AC7). Figure 14 illustrates the specific surface area and pore volume of activated char obtained from different O_2/C conditions. With the increase of the concentration of O_2/C, the specific surface area of the mesoporous region increases first and then decreases, while the specific pore volume of the mesoporous region increases all the time. This indicates that the increase in the level of O_2/C promotes the formation and development of mesoporous. The

https://doi.org/10.1021/acsomega.4c00467
ACS Omega 2024, 9, 24500−24512

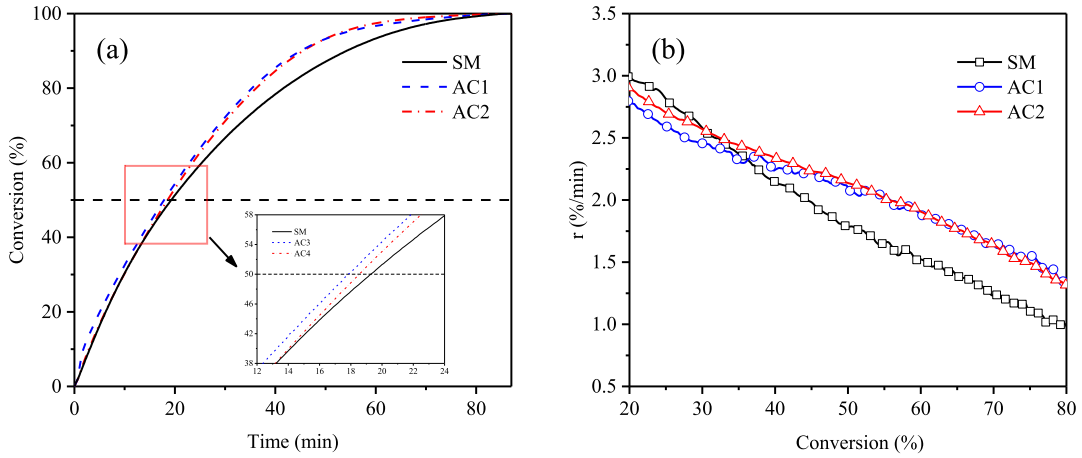

Figure 9. Carbon conversion curves with time (a) and reaction rates with carbon conversion (b) of SM, AC1, and AC2.

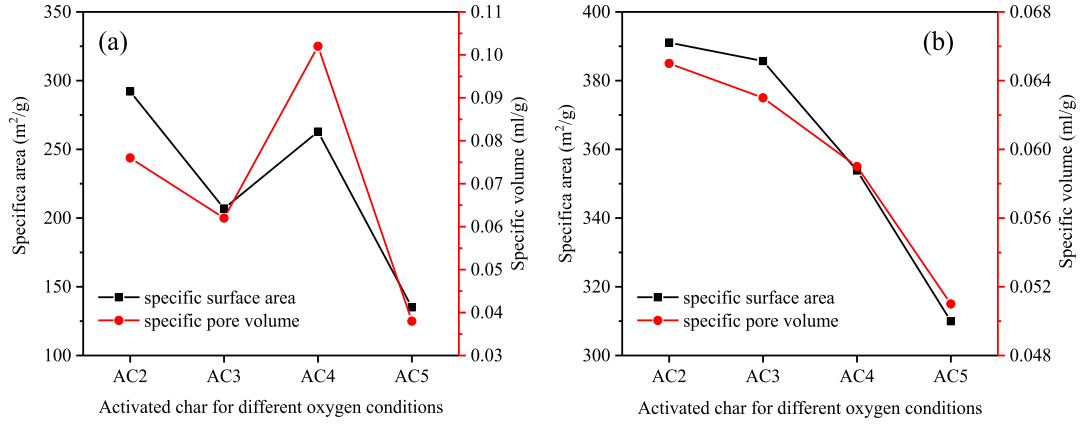

Figure 10. Specific surface area and the specific pore volume of activated char obtained from different oxygen concentration conditions (a) mesopore and (b) micropore.

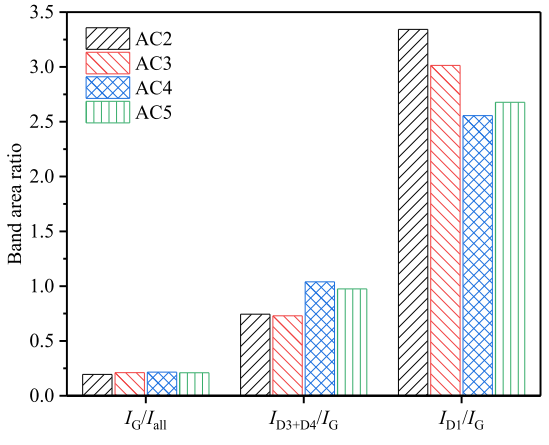

Figure 11. Variation of band area ratios of activated char obtained from different oxygen concentration conditions.

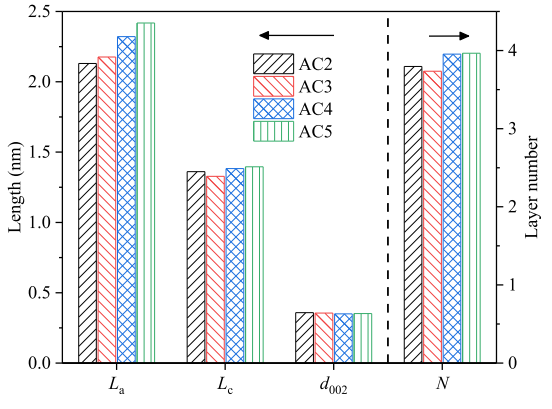

Figure 12. Crystal lattice parameters of activated char obtained from different oxygen concentration conditions.

specific surface area and the specific pore volume of micropores decrease with the increase of O_2/C. From the trend of mesoporous changes, this may be due to the increase of O_2/C promoting the development of micropore pore size, and more micropores being transformed into mesoporous pores. This transformation mechanism is obvious when the amount of O_2/C increases from 0.25 to 0.35, and the further increase of the amount of O_2/C does not significantly promote the development of mesoporous pores, and the micropores are still disappearing. This indicates that the original mesoporous hole begins to disappear and the hole collapses. It is worth noticing that the operating temperature and oxygen concentration in different conditions are similar. The effect of O_2/C on the pore structure of activated char is mainly caused by changing the carbon content.

Figure 15 shows the fitting analysis results of the Raman spectra of activated char obtained from different O_2/C conditions. With the increase in the level of O_2/C, the graphitization degree of activated char is basically the same.

https://doi.org/10.1021/acsomega.4c00467
ACS Omega 2024, 9, 24500−24512

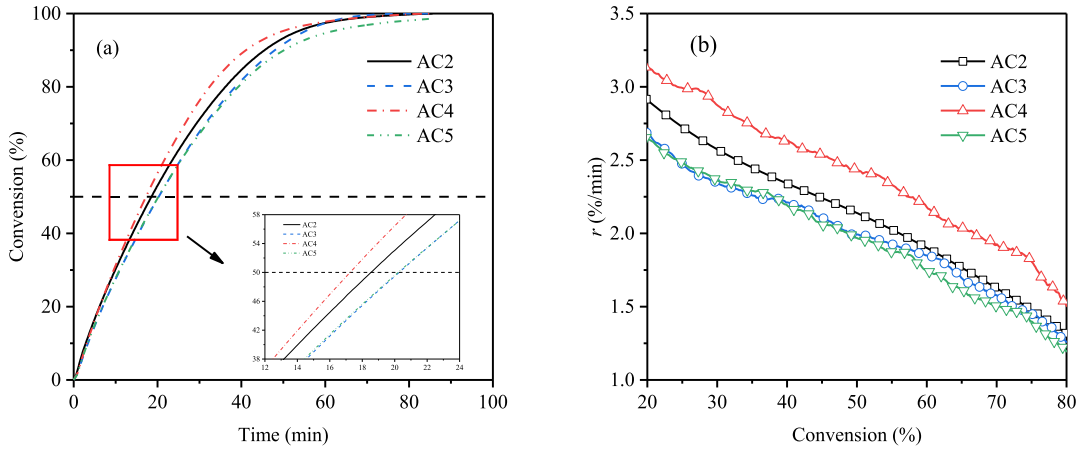

Figure 13. Carbon conversion curves with time (a) and reaction rates with carbon conversion (b) of activated char obtained from different oxygen concentration conditions.

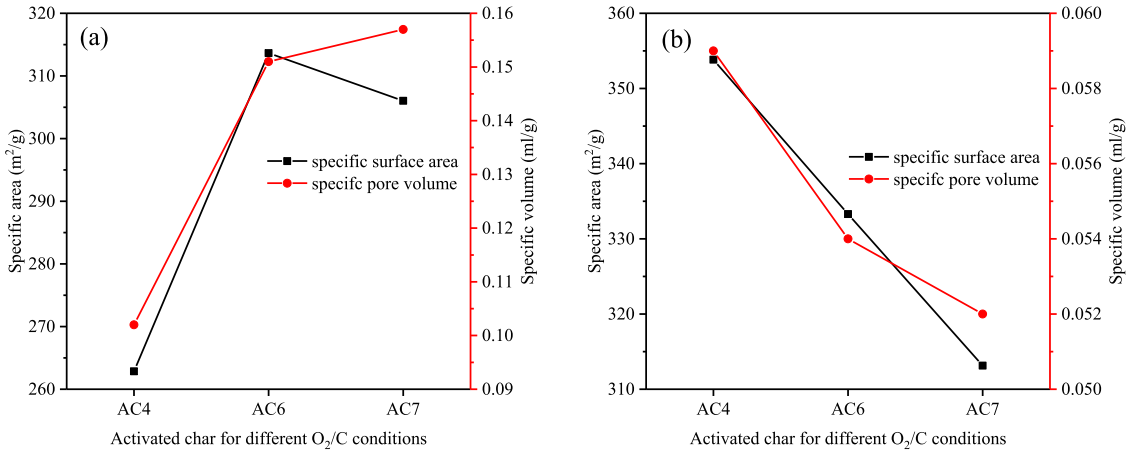

Figure 14. Specific surface area and the specific pore volume of activated char obtained from different O_2/C conditions: (a) mesopore and (b) micropore.

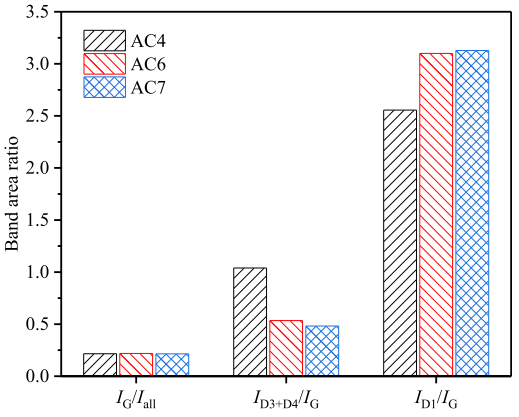

Figure 15. Variation of band area ratios of activated char obtained from different O_2/C conditions.

When the level of the ion concentration of the O_2/C increases from 0.25 to 0.35, the I_{D3+D4}/I_G significantly decreases and a further increase in the level of the O_2/C has a smaller impact on the I_{D3+D4}/I_G, while the trend of I_{D1}/I_G is opposite. It can be considered that with the enhancement of combustion reaction, the active sites on the mesoporous surface are consumed significantly while the mesoporous surface is expanded, and the in-surface defects increase. However, when the combustion reaction is increased to a certain extent, the mesoporous properties and graphite microcrystalline properties of activated semicoke will remain stable. Therefore, a further increase in the level of O_2/C hardly affects the mesoporous characteristics and I_{D3+D4}/I_G. The possible mechanism is that the initial stage of the enhanced combustion reaction ($0.25 < O_2/C < 0.35$) consumes the active site generated by the Boudouard reaction. In the later stage of enhanced combustion ($0.35 < O_2/C$), few of the active sites generated by the Boudouard reaction remain. At this point, the combustion reaction produces and consumes the active site; two competing mechanisms reach a balance.

Figure 16 shows the XRD results of activated char obtained under different O_2/C conditions. As the O_2/C increases, the average string length of the aromatic layer (L_a) in the activated char decreases. It is probably because the graphite microcrystals, which are smaller in activated carbon, are more inclined to react in the reaction and thus consume. Combined with the results of Raman spectroscopy, it can be suggested that I_{D3+D4}/I_G may be associated with L_a rather than I_{D1}/I_G as in the previous results.[31] This may be due to the fact that the L_a of activated char is too small to form the relationship between L_a and I_{D1}/I_G. The correlation of I_{D3+D4}/I_G with L_a may be related to the sp^2 hybridization and the sp^2–sp^3 hybridization at the edges of the microcrystals; i.e., larger sheet size corresponds to smaller "perimeter/area".

https://doi.org/10.1021/acsomega.4c00467
ACS Omega 2024, 9, 24500−24512

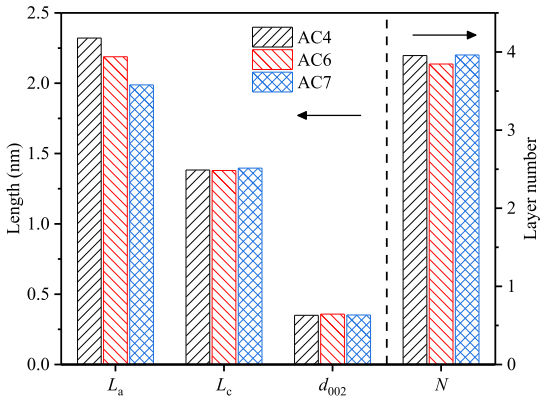

Figure 16. Crystal lattice parameters of activated char obtained from different conditions of the O_2/C conditions.

Figure 17 shows the thermogravimetric experiment results of activated char obtained under different O_2/C conditions. With the increase of the level of O_2/C, the reactivity of activated char decreases gradually, and AC4 has the best reactivity among these activated chars. The reactivity of activated char is similar to the characteristics of variation of I_{D3+D4}/I_G, which is consistent with the reactivity of activated char obtained from the different oxygen concentration conditions. The lower O_2/C results in better reactivity of activated char, which is because of the more active sites. In addition, the reactivity of activated char and the characteristics of micropores are also relevant. There are various factors that affect the reactivity of activated char.

3.4. Relationship between Reactivity and Structure Properties. Various parameters, such as specific surface area, specific pore volume, I_G/I_{all}, L_a, etc., have been used to describe the physical and chemical properties of activated char. The variety of parameters makes it difficult to directly show the relationship between each parameter and the reactivity of activated char. Therefore, the results of each parameter of activated char are summarized, and a correlation analysis is carried out on the reactivity of activated char. The reactivity of activated char is characterized by $R_{0.5}$, which is calculated as follows:

$$R_{0.5} = 0.5/t_{0.5} \quad (8)$$

where $t_{0.5}$ is the time required to reach 50% carbon conversion.

Figure 18 shows the relationship between $R_{0.5}$ and the mesoporous specific surface area or specific pore volume. It can be found that two regions are formed in Figure 18a. Zone A and Zone B are bound by 260 m^2/g. The points with higher $R_{0.5}$ are all in Zone B. Accordingly, the points in Zone A have the lower mesoporous specific surface area and their $R_{0.5}$ is at a lower position. This means that the mesoporous specific surface area has an important effect on the reactivity of the activated char. However, although the points in Zone B have a large mesoporous specific surface area, their $R_{0.5}$ is not all high. Some of these points, while having large mesoporous surface areas, still have poor reactivity. And they are at a similar level to the points in Zone A. This indicates that the large mesoporous specific surface area of activated char is necessary for high reactivity, but the mesoporous specific surface area does not seem to completely determine the reactivity. The points of different oxygen concentration conditions and the points of different O_2/C conditions show a well-linear correlation. The reactivity of activated char is significantly affected by the mesoporous specific pore volume, which is changed by oxygen concentrations. The results of specific surface area and specific pore volume indicate that the diffusion of CO_2 molecules in mesopores seems to be more important.[32] Therefore, it is necessary that the mesoporous is large enough for the occurrence of a Boudouard reaction so that CO_2 can contact and react with the active site on the mesoporous surface.[33] However, the reactivity is not entirely determined by the mesoporous specific pore volume. In this regard, the role of the mesoporous specific pore volume is similar to that of the mesoporous specific surface area.

Figure 19 shows the relationship between $R_{0.5}$ and micropore specific surface area or specific pore volume. The relationship between microporous specific surface area and $R_{0.5}$ is divided into two regions, Zone A and Zone B. In both zones, the ratio of $R_{0.5}$ to microporous is negatively correlated. The negative correlation in Zone B is smaller and the slope is closer to 0. However, the negative correlation in Zone A is more obvious and the slope is larger. This relationship is induced by the transition of micropores into mesopores during the activation process. In this process, the specific surface area of the micropore gradually decreases, and the specific pore volume of the mesoporous gradually increases, leading to the

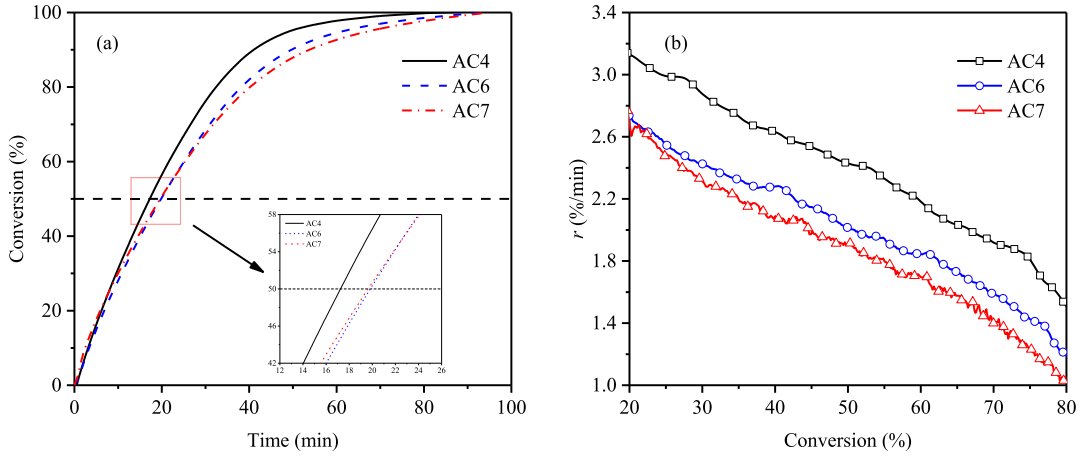

Figure 17. Carbon conversion curves with time (a) and reaction rates with carbon conversion (b) of activated char obtained from different O_2/C conditions.

https://doi.org/10.1021/acsomega.4c00467
ACS Omega 2024, 9, 24500−24512

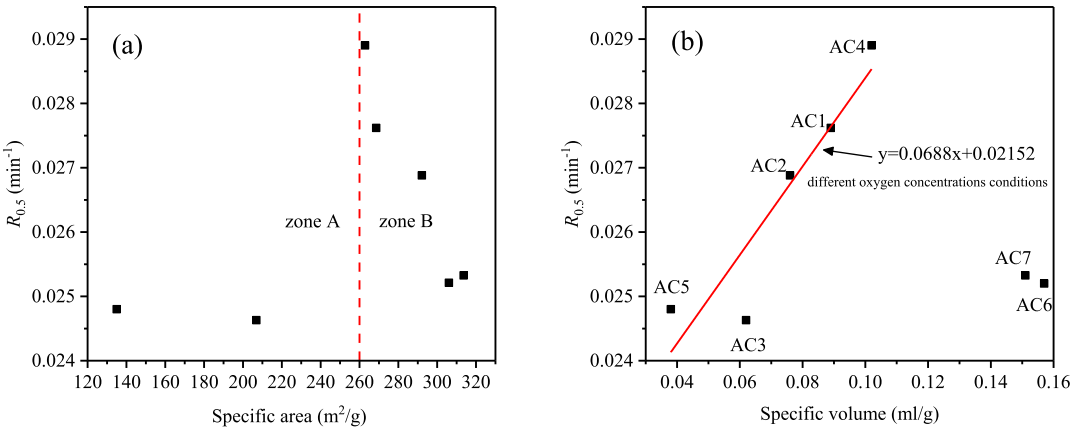

Figure 18. Relationship between the mesoporous structure and $R_{0.5}$ (a) specific surface area and (b) specific pore volume.

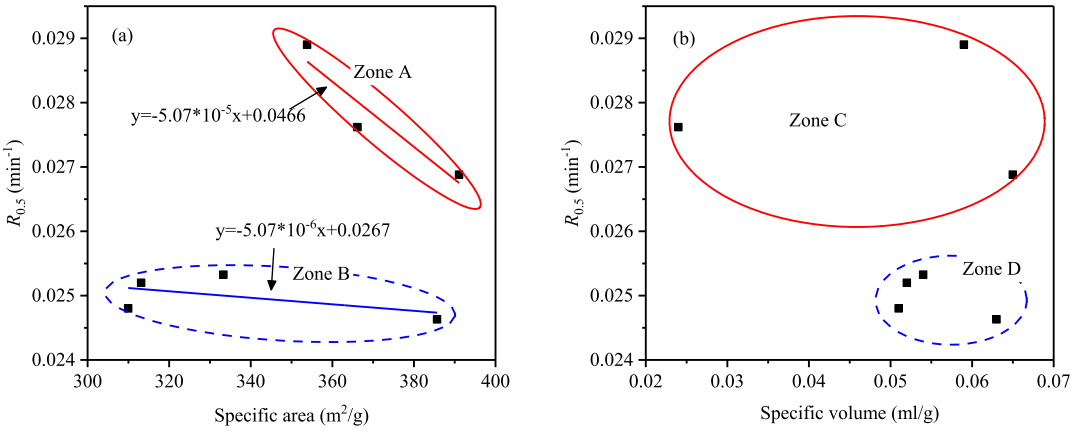

Figure 19. Relationship between the micropore structure and $R_{0.5}$ (a) specific surface area and (b) specific volume.

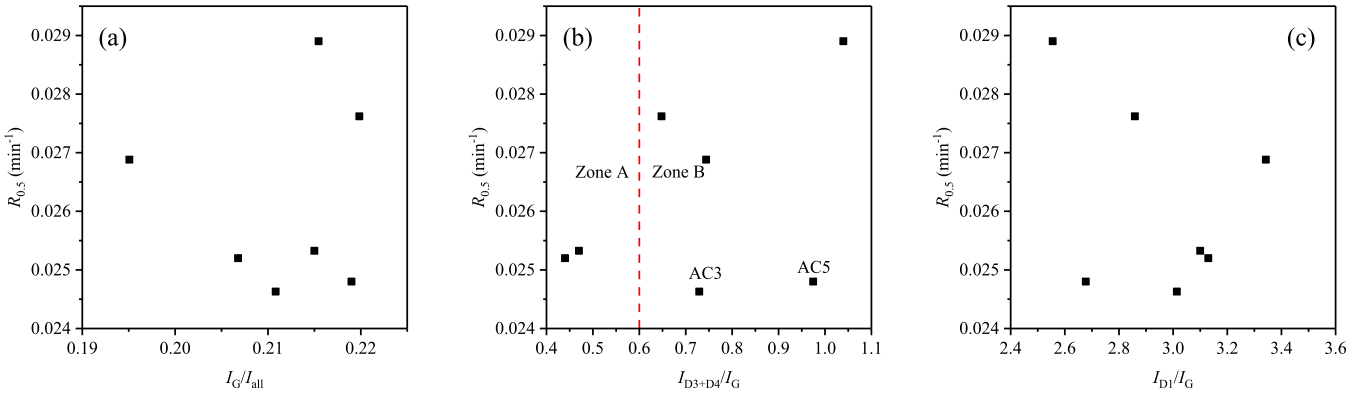

Figure 20. Relationship of the fitting analysis result of I_G/I_{all} (a), I_{D3+D4}/I_G (b), I_{D1}/I_G, and $R_{0.5}$ (c).

enhancement of the reactivity of activated char. The relationship between the specific pore volume of micropores and the $R_{0.5}$ can be divided into Zone C and Zone D. There is no obvious rule in the distribution of the inner points in both zones. $R_{0.5}$ of points in Zone is larger, compared to Zone D. The relationship in the four zones in Figure 19 suggests that the micropores of activated char do not seem to be the main place of the Boudouard reaction.[32,34] The effect of micropores on the reaction is mainly reflected in the degree of the transition of the micropore to the mesoporous.

Figure 20 shows the relationship of the fitting analysis results of Raman and $R_{0.5}$. There is no good correlation between the $R_{0.5}$ and Raman parameters. The distribution of $R_{0.5}$ in each subsection is scattered. Among them, I_{D3+D4}/I_G has a good correlation with $R_{0.5}$, excluding AC3 and AC5. This indicates that the active site represented by I_{D3+D4}/I_G has a great influence on the reactivity of the activated char. According to Figure 10a, it can be observed that the mesoporous specific surface area of AC3 and AC5 is significantly lower than that of the remaining activated char. One possible reason is that I_{D3+D4}/I_G is related to the density of the active sites rather than the total amount. When the mesoporous specific surface area of AC3 and AC5 is small, the total number of corresponding active sites is also low. In addition, Figure 20b can be divided into two zones, Zone A and Zone B. It can be observed that the sites with higher reactivity are all in region B, and these

https://doi.org/10.1021/acsomega.4c00467
ACS Omega 2024, 9, 24500−24512

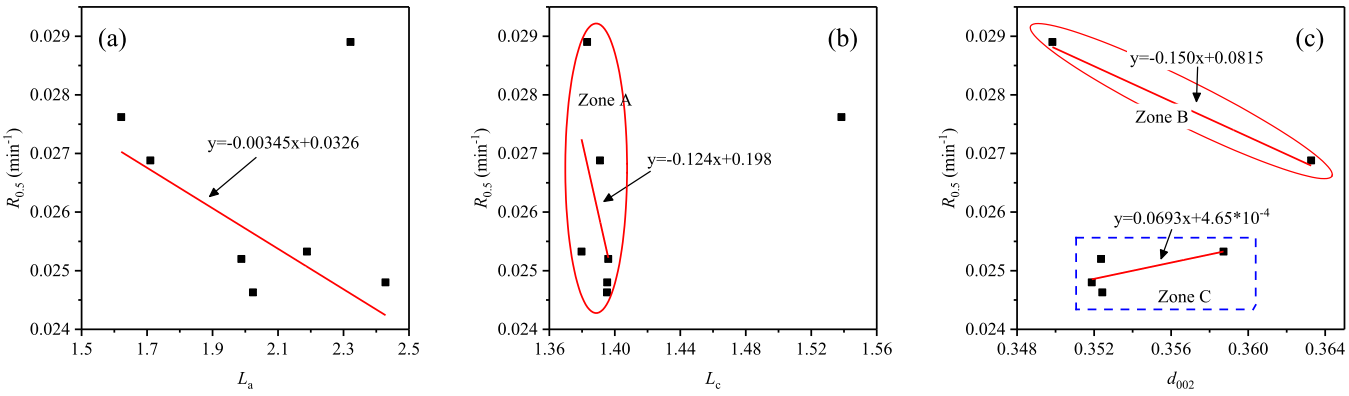

Figure 21. Relationship of the analysis result of the XRD and $R_{0.5}$ (a) L_a (b) L_c (c) d_{002}.

sites have higher I_{D3+D4}/I_G. This indicates that the mesoporous surface area of I_{D3+D4}/I_G is similar to that of activated char, which is a necessary condition.

Figure 21 shows the relationship between the fitting analysis result of XRD and $R_{0.5}$. $R_{0.5}$ as a whole showed a negative correlation with L_a and L_c. This coincides with the physical significance of the parameters represented by L_a and L_c. The correlations of d_{002} with $R_{0.5}$ are not significant. The nonunique relationship between d_{002} and $R_{0.5}$ is represented in Figure 21c, divided into Zone B and Zone C. The distribution of points in Zone B indicates a negative correlation between d_{002} and $R_{0.5}$, while the distribution of points in Zone C suggests that d_{002} is not strongly related to $R_{0.5}$. The point distribution in Zone B shows a negative correlation between $R_{0.5}$ and d_{002}, which is inconsistent with the representation of d_{002}.[27,35] The reason for this condition may be the fact that other parameters determine the distribution of points.

The above simple parameters do not characterize the reactivity of the activated char well. Based on the analysis results, it seems that the reactivity of activated char is difficult to characterize by a single simple parameter. The sufficient mesoporous specific surface area and sufficient I_{D3+D4}/I_G are the necessary conditions for the high reactivity of activated char. However, the correlation between them and the reactivity is not good. Based on the widely accepted oxygen exchange mechanism,[36] the active surface area (*ASA*) is a key parameter that affects the reactivity.[37,38] However, there is no general measurement method to evaluate this parameter. At present, the commonly used methods to characterize this parameter include CO_2 chemisorption device measurement[39] and thermogravimetric equipment measurement by examining the mass change in the adsorption and desorption process of CO_2 and other gases.[6,38,40] However, the above two methods have problems such as small adsorption amounts, difficulty in effectively measuring, and strict requirements for the decomposition of raw materials, such as tar content, used in testing equipment.

Therefore, based on the physical meaning of *ASA*, reactive specific surface area (*RSSA*) is used, which is calculated as follows:

$$RSSA = MSSA_{BET} \cdot I_{D_3+D_4}/I_{all} \quad (9)$$

where $MSSA_{BET}$ (mesoporous specific surface area) represents the mesoporous specific surface area of activated char, which is determined by N_2 as the measuring medium and calculated by the BET method, and contains both active and inert surfaces. I_{D3+D4}/I_{all}, obtained by fitting Raman results, is the ratio of the area of the D_3 + D_4 peaks to the total Raman area, which represents the proportion of the area occupied by the active sites to the total area. I_{D3+D4}/I_G is sometimes greater than 1 (Figure 20b), which is unacceptable for the characterizing ratio. Also, the physical meaning of I_{D3+D4}/I_G is not intuitive. Therefore, the I_{D3+D4}/I_{all} characterization is used.

The correlation between *RSSA* and $R_{0.5}$ is shown in Figure 22. It can be observed that *RSSA* has a better correlation with

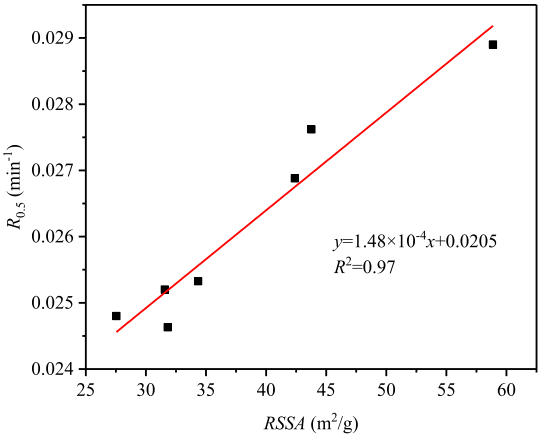

Figure 22. Relationship of the analysis result of *RSSA* and $R_{0.5}$.

$R_{0.5}$ than other simple parameters, with R^2 reaching 0.92. It shows that *RSSA* is better than other simple parameters in describing the reactivity of activated char.

4. CONCLUSIONS

The activation process in CFB was investigated on a 20 kg/h self-heating activated-reduction test rig. In order to investigate the effects of the activation process and obtain the effects of different activation conditions on the physicochemical properties of activated char, CO_2 addition, oxygen concentration, and O_2/C on the physicochemical properties of activated char were studied. By analysis of the distribution of data points, *RSSA* was proposed to characterize the reactivity. The main conclusions are as follows:

1. The pore structure of activated char is fully developed, and the degree of graphitization decreases with the increase in the number of active sites during the CFB activation process, thus leading to a higher reactivity of activated char than that of raw coal.

https://doi.org/10.1021/acsomega.4c00467
ACS Omega 2024, 9, 24500−24512

2. Under similar O_2/C, activated char obtained from a 40% oxygen concentration condition has the best reactivity. This is mainly because activated char has good mesoporous characteristics, the number of active sites represented by D_3 and D_4 is large, and the degree of graphitization is low. Under similar oxygen concentrations, for the same reasons, activated char obtained from the lower O_2/C conditions has the best reactivity.
3. Sufficient mesoporous surface area and sufficient I_{D3+D4}/I_G are the necessary conditions for the high reactivity of activated char. However, the correlation between them and the reactivity is not good. *RSSA* was proposed to characterize the reactivity and it is better than other simple parameters in describing the reactivity.

AUTHOR INFORMATION

Corresponding Author

Chen Liang − *Institute of Engineering Thermophysics, Chinese Academy of Sciences, Beijing 100190, China*; Email: liangchen@iet.cn

Authors

Siyuan Zhang − *Institute of Engineering Thermophysics, Chinese Academy of Sciences, Beijing 100190, China; University of Chinese Academy of Sciences, Beijing 100049, China*; orcid.org/0000-0002-2121-4716

Mingyue Wang − *Institute of Engineering Thermophysics, Chinese Academy of Sciences, Beijing 100190, China*

Zhiping Zhu − *Institute of Engineering Thermophysics, Chinese Academy of Sciences, Beijing 100190, China; University of Chinese Academy of Sciences, Beijing 100049, China; State Key Laboratory of Coal Conversion, Institute of Engineering Thermophysics, Chinese Academy of Sciences, Beijing 100190, China*

Complete contact information is available at: https://pubs.acs.org/10.1021/acsomega.4c00467

Notes

The authors declare no competing financial interest.

ACKNOWLEDGMENTS

This work was supported by the Strategic Priority Research Program of the Chinese Academy of Sciences, Grant No. XDA 29030100.

REFERENCES

(1) Roncancio, R.; Gore, J. P. CO2 char gasification: A systematic review from 2014 to 2020. *Energy Conversion and Management: X* **2021**, *10*, No. 100060.

(2) Zhuang, W.; Song, X.; Liu, M.; Wang, Q.; Song, J.; Duan, L.; Li, X.; Yuan, H. Potential capture and conversion of CO2 from oceanwater through mineral carbonation. *Science of The Total Environment* **2023**, *867*, No. 161589.

(3) Medrano-García, J. D.; Ruiz-Femenia, R.; Caballero, J. A. Optimal carbon dioxide and hydrogen utilization in carbon monoxide production. *Journal of CO2 Utilization* **2019**, *34*, 215−230.

(4) Chan, Y. H.; Syed Abdul Rahman, S. N. F.; Lahuri, H. M.; Khalid, A. Recent progress on CO-rich syngas production via CO2 gasification of various wastes: A critical review on efficiency, challenges and outlook. *Environ. Pollut.* **2021**, *278*, No. 116843.

(5) Hunt, J.; Ferrari, A.; Lita, A.; Crosswhite, M.; Ashley, B.; Stiegman, A. E. Microwave-Specific Enhancement of the Carbon−Carbon Dioxide (Boudouard) Reaction. *J. Phys. Chem. C* **2013**, *117* (51), 26871−26880.

(6) Jing, X.; Wang, Z.; Zhang, Q.; Yu, Z.; Li, C.; Huang, J.; Fang, Y. Evaluation of CO2 Gasification Reactivity of Different Coal Rank Chars by Physicochemical Properties. *Energy Fuels* **2013**, *27* (12), 7287−7293.

(7) Lahijani, P.; Zainal, Z. A.; Mohamed, A. R.; Mohammadi, M. CO2 gasification reactivity of biomass char: Catalytic influence of alkali, alkaline earth and transition metal salts. *Bioresour. Technol.* **2013**, *144*, 288−295. Malekshahian, M.; Hill, J. M. Potassium catalyzed CO2 gasification of petroleum coke at elevated pressures. *Fuel Process. Technol.* **2013**, *113*, 34−40.

(8) Lahijani, P.; Zainal, Z. A.; Mohammadi, M.; Mohamed, A. R. Conversion of the greenhouse gas CO2 to the fuel gas CO via the Boudouard reaction: A review. *Renewable and Sustainable Energy Reviews* **2015**, *41*, 615−632.

(9) Liang, C.; Wang, X.; Lyu, Q. Experimental investigation on fluidized modification in gasification of preheated coal using oxygen and steam. *Fuel* **2021**, *304*, No. 121375.

(10) Zhang, Y.; Zhu, J. G.; Lyu, Q. G.; Pan, F. Experimental Study on Combustion Characteristics of Pulverized Coal Based on Partial Gasification of Circulating Fluidized Bed. *ENERGY & FUELS* **2020**, *34* (1), 989−995.

(11) Liu, Y.; Liu, J.; Lyu, Q.; Zhu, J.; Zhang, X.; Zhang, J.; Cao, X. Comparison of oxy-fuel preheated combustion characteristics of high- and low- volatility carbon-based fuels. *Fuel* **2022**, *330*, No. 125583.

(12) Zhang, Y.; Zhu, J.; Lyu, Q.; Liu, J.; Pan, F.; Zhang, J. The ultra-low NOx emission characteristics of pulverized coal combustion after high temperature preheating. *Fuel* **2020**, *277*, No. 118050. Zhang, Y.; Zhu, J.; Lyu, Q.; Liu, J.; Pan, F. Coke generation and conversion behavior of pulverized coal combustion. *Journal of the Energy Institute* **2020**, *93* (5), 2096−2107. Zhang, X.; Zhu, S.; Zhu, J.; Liu, Y.; Zhang, J.; Hui, J.; Ding, H.; Cao, X.; Lyu, Q. Preheating and combustion characteristics of anthracite under O2/N2, O2/CO2 and O2/CO2/H2O atmospheres. *Energy* **2023**, *274*, No. 127419.

(13) Su, K.; Ouyang, Z.; Ding, H.; Wang, W.; Zhang, J.; Wang, H.; Zhu, S. Experimental investigation on effect of external circulation system on preheating characteristics of pulverized coal. *Energy* **2023**, *278*, No. 127781.

(14) Ding, H.; Ouyang, Z.; Shi, Y.; Chen, R.; Zhang, Z.; Zhu, S.; Lyu, Q. Effects of the T-abrupt exit configuration of riser on fuel properties, combustion characteristics and NOx emissions with coal self-preheating technology. *Fuel* **2023**, *337*, No. 126860.

(15) Qi, X.; Yang, Q.; Song, W.; Zhu, Z.; Lyu, Q. Experimental study and theoretical analysis on fluidized activation of coal gasification fly ash from an industrial CFB gasifier. *Waste Management* **2023**, *157*, 82−90.

(16) Li, J.; Chen, Z.; Li, L.; Qiao, Y.; Yuan, Z.; Zeng, L.; Li, Z. Study on pore and chemical structure characteristics of atmospheric circulating fluidized bed coal gasification fly ash. *Journal of Cleaner Production* **2021**, *308*, No. 127395.

(17) Yang, Q.; Qi, X.; Lyu, Q.; Zhu, Z. Physicochemical Properties of Coal Gasification Fly Ash from Circulating Fluidized Bed Gasifier. *Journal of Thermal Science* **2023**, *32* (4), 1710−1720.

(18) Jiang, J.; Zhang, S.; Longhurst, P.; Yang, W.; Zheng, S. Molecular structure characterization of bituminous coal in Northern China via XRD, Raman and FTIR spectroscopy. *Spectrochimica Acta Part A: Molecular and Biomolecular Spectroscopy* **2021**, *255*, No. 119724.

(19) Liu, H.; Chen, T.; Fang, L. Evolution of char structure during non-isothermal low temperature pyrolysis of ZhunDong coal by microwave heating: A comparative study with conventional heating. *Journal of the Energy Institute* **2020**, *93* (3), 1195−1206.

(20) Zaida, A.; Bar-Ziv, E.; Radovic, L. R.; Lee, Y.-J. Further development of Raman Microprobe spectroscopy for characterization of char reactivity. *Proceedings of the Combustion Institute* **2007**, *31* (2), 1881−1887. Liu, X.; Zheng, Y.; Liu, Z.; Ding, H.; Huang, X.; Zheng, C. Study on the evolution of the char structure during hydrogasification process using Raman spectroscopy. *Fuel* **2015**, *157*, 97−106.

(21) Sheng, C. Char structure characterised by Raman spectroscopy and its correlations with combustion reactivity. *Fuel* **2007**, *86* (15), 2316−2324.
(22) Liu, Y.; Liu, J.; Lyu, Q.; Zhu, J.; Pan, F. Microstructure analysis of fluidized preheating pulverized coal under O2/CO2 atm. *Fuel* **2021**, *292*, No. 120386.
(23) Guedes, A.; Valentim, B.; Prieto, A. C.; Noronha, F. Raman spectroscopy of coal macerals and fluidized bed char morphotypes. *Fuel* **2012**, *97*, 443−449.
(24) Takagi, H.; Maruyama, K.; Yoshizawa, N.; Yamada, Y.; Sato, Y. XRD analysis of carbon stacking structure in coal during heat treatment. *Fuel* **2004**, *83* (17), 2427−2433.
(25) Gubernat, M.; Fraczek-Szczypta, A.; Tomala, J.; Blazewicz, S. Catalytic effect of montmorillonite nanoparticles on thermal decomposition of coal tar pitch to carbon. *Journal of Analytical and Applied Pyrolysis* **2018**, *130*, 90−98.
(26) Hemmati-Sarapardeh, A.; Dabir, B.; Ahmadi, M.; Mohammadi, A. H.; Husein, M. M. Toward mechanistic understanding of asphaltene aggregation behavior in toluene: The roles of asphaltene structure, aging time, temperature, and ultrasonic radiation. *J. Mol. Liq.* **2018**, *264*, 410−424. Sharma, A.; Kyotani, T.; Tomita, A. Comparison of structural parameters of PF carbon from XRD and HRTEM techniques. *Carbon* **2000**, *38* (14), 1977−1984. Yan, J.; Lei, Z.; Li, Z.; Wang, Z.; Ren, S.; Kang, S.; Wang, X.; Shui, H. Molecular structure characterization of low-medium rank coals via XRD, solid state 13C NMR and FTIR spectroscopy. *Fuel* **2020**, *268*, No. 117038.
(27) Liu, M.; He, Q.; Bai, J.; Yu, J.; Kong, L.; Bai, Z.; Li, H.; He, C.; Cao, X.; Ge, Z.; et al. Char reactivity and kinetics based on the dynamic char structure during gasification by CO2. *Fuel Process. Technol.* **2021**, *211*, No. 106583.
(28) Wu, S.; Huang, S.; Ji, L.; Wu, Y.; Gao, J. Structure characteristics and gasification activity of residual carbon from entrained-flow coal gasification slag. *Fuel* **2014**, *122*, 67−75.
(29) Dippel, B.; Jander, H.; Heintzenberg, J. NIR FT Raman spectroscopic study of flame soot. *Phys. Chem. Chem. Phys.* **1999**, *1* (20), 4707−4712. Jawhari, T.; Roid, A.; Casado, J. Raman spectroscopic characterization of some commercially available carbon black materials. *Carbon* **1995**, *33* (11), 1561−1565.
(30) Wang, Y.; Alsmeyer, D. C.; McCreery, R. L. Raman spectroscopy of carbon materials: structural basis of observed spectra. *Chem. Mater.* **1990**, *2* (5), 557−563.
(31) Tuinstra, F.; Koenig, J. L. Raman Spectrum of Graphite. *J. Chem. Phys.* **2003**, *53* (3), 1126−1130.
(32) Scott, S. A.; Davidson, J. F.; Dennis, J. S.; Fennell, P. S.; Hayhurst, A. N. The rate of gasification by CO2 of chars from waste. *Proceedings of the Combustion Institute* **2005**, *30* (2), 2151−2159.
(33) Kim, Y. T.; Seo, D. K.; Hwang, J. Study of the Effect of Coal Type and Particle Size on Char−CO2 Gasification via Gas Analysis. *Energy Fuels* **2011**, *25* (11), 5044−5054.
(34) Hurt, R. H.; Sarofim, A. F.; Longwell, J. P. The role of microporous surface area in the gasification of chars from a sub-bituminous coal. *Fuel* **1991**, *70* (9), 1079−1082.
(35) Diao, R.; Zhu, X.; Wang, C.; Zhu, X. Synergistic effect of physicochemical properties and reaction temperature on gasification reactivity of walnut shell chars. *Energy Conversion and Management* **2020**, *204*, No. 112313.
(36) Ergun, S. Kinetics of the Reaction of Carbon with Carbon Dioxide. *J. Phys. Chem.* **1956**, *60* (4), 480−485.
(37) Radović, L. R.; Walker, P. L.; Jenkins, R. G. Importance of carbon active sites in the gasification of coal chars. *Fuel* **1983**, *62* (7), 849−856.
(38) Xu, K.; Hu, S.; Su, S.; Xu, C.; Sun, L.; Shuai, C.; Jiang, L.; Xiang, J. Study on Char Surface Active Sites and Their Relationship to Gasification Reactivity. *Energy Fuels* **2013**, *27* (1), 118−125.
(39) Molina, A.; Montoya, A.; Mondragón, F. CO2 strong chemisorption as an estimate of coal char gasification reactivity. *Fuel* **1999**, *78* (8), 971−977.
(40) Zhang, Y.; Hara, S.; Kajitani, S.; Ashizawa, M. Modeling of catalytic gasification kinetics of coal char and carbon. *Fuel* **2010**, *89* (1), 152−157. Guizani, C.; Escudero Sanz, F. J.; Jeguirim, M.; Gadiou, R.; Salvador, S. The effects of textural modifications on beech wood-char gasification rate under alternate atmospheres of CO2 and H2O. *Fuel Process. Technol.* **2015**, *138*, 687−694.

NOTE ADDED AFTER ASAP PUBLICATION

This paper originally published ASAP on May 28, 2024. Figures 2 and 8 were modified and reposted later the same day.

https://doi.org/10.1021/acsomega.4c00467
ACS Omega 2024, 9, 24500−24512